Biofilm compressibility in ultrafiltration

A relation between biofilm morphology, mechanics and hydraulic resistance

Jafari, Morez; Derlon, Nicolas; Desmond, Peter; van Loosdrecht, Mark C.M.; Morgenroth, Eberhard; Picioreanu, Cristian

DOI
10.1016/j.watres.2019.03.073

Publication date
2019

Document Version
Final published version

Published in
Water Research

Citation (APA)
Jafari, M., Derlon, N., Desmond, P., van Loosdrecht, M. C. M., Morgenroth, E., & Picioreanu, C. (2019). Biofilm compressibility in ultrafiltration: A relation between biofilm morphology, mechanics and hydraulic resistance. *Water Research*, *157*, 335-345. https://doi.org/10.1016/j.watres.2019.03.073

Water Research 157 (2019) 335–345

Contents lists available at ScienceDirect

Water Research

journal homepage: www.elsevier.com/locate/watres

Biofilm compressibility in ultrafiltration: A relation between biofilm morphology, mechanics and hydraulic resistance

Morez Jafari [a, *], Nicolas Derlon [b], Peter Desmond [b, c], Mark C.M. van Loosdrecht [a], Eberhard Morgenroth [b, c], Cristian Picioreanu [a]

[a] Department of Biotechnology, Faculty of Applied Sciences, Delft University of Technology, Van der Maasweg 9, 2629 HZ, Delft, the Netherlands
[b] Eawag, Swiss Federal Institute of Aquatic Science and Technology, 8600, Dübendorf, Switzerland
[c] ETH Zürich, Institute of Environmental Engineering, 8093, Zürich, Switzerland

ARTICLE INFO

Article history:
Received 6 December 2018
Received in revised form
22 February 2019
Accepted 1 March 2019
Available online 2 April 2019

Keywords:
Biofilm compression
Hydraulic resistance
Poroelastic model
Biofilm surface roughness
Membrane filtration

ABSTRACT

Poroelastic fluid-structure interaction models were coupled to experimental data to determine the effects of biofilm spatial distribution of mechanical and hydraulic properties on the biofilm hydraulic resistance and compressibility in membrane filtration processes. Biofilms were cultivated on ultrafiltration membranes for 20 and 30 days under high (0.28 bar) and low (0.06 bar) transmembrane pressure (TMP), in dead-end filtration mode. Subsequently, biofilms were subjected to a compression/relaxation cycles by step-wise TMP changes. Structural deformation of biofilms during compression was observed *in-situ* using optical coherence tomography.

Experimental results show that the observed increase in the biofilm hydraulic resistance during compression is not necessarily accompanied by a detectable biofilm thickness reduction. A dual-layer biofilm model with a dense base and porous top layer could explain these observed results. Because porosity controls indirectly the mechanical response of biofilms under compression, results could be described without assuming a gradient in mechanical properties within the biofilm. The biofilm surface roughness did not significantly influence the water flux in this study. However, the fraction of biofilm base layer directly exposed to bulk liquid could be a good indicator in the determination of water flux. The main implications of this study for the design and operation of low-pressure membrane systems (e.g., MF and UF with fouling layer being the main filtration resistance) lays in the selection of favorable operational TMP and biofilm morphology.

1. Introduction

Biofilm formation causes additional hydraulic resistance that adversely impacts water production in membrane systems (McDonogh et al., 1994; Radu et al., 2010). In membrane systems such as microfiltration (MF) and ultrafiltration (UF), biofilm resistance is the main filtration resistance (Dreszer et al., 2013; Ko and Pellegrino, 1992; Martin et al., 2014). Biofilms are often described as porous media consisting of several layers with different properties, such as density (Zhang and Bishop, 1994), porosity (Gao et al., 2011a; Okabe et al., 1998; Rosenthal et al., 2018) and elastic modulus (Aravas and Laspidou, 2008; Picioreanu et al., 2018). In general, biofilm porosity increases with the distance from substratum, whereas the biofilm elastic modulus (or rigidity) seems to have an opposite trend.

The spatial distribution of porosity and mechanical properties affect the biofilm permeability, as well as the structural responses under compressive forces. Biofilm compression has been often described as the main cause of changes in biofilm hydraulic resistance during water filtration (Derlon et al., 2016; Dreszer et al., 2013; Jorgensen et al., 2017; Poorasgari et al., 2016; Valladares Linares et al., 2015). Indeed, as biofilms are subjected to larger forces (e.g., higher transmembrane pressure, TMP) biofilms undergo a decrease in thickness and surface roughness (Derlon et al. 2014, 2016; Desmond et al., 2018c; Dreszer et al., 2014; Valladares Linares et al., 2015) leading to a reduction in biofilm porosity (Blauert et al., 2015) and permeability (Derlon et al., 2016; Desmond et al., 2018c). The magnitude of the increase in hydraulic resistance upon compression depends on biofilm composition (e.g., EPS concentration and composition) (Desmond et al., 2018a;

* Corresponding author. Van der Maasweg, 9, 2629 HZ, Delft, the Netherlands.
E-mail address: M.Jafarieshlaghi@tudelft.nl (M. Jafari).

https://doi.org/10.1016/j.watres.2019.03.073
0043-1354/

Herzberg et al., 2009), growth conditions (e.g., operational TMP and growth time) (Derlon et al., 2016; Dreszer et al., 2014; Poorasgari et al., 2015) and operation mode (e.g., dead-end and cross flow). Poorasgari et al. (2015) reported an increased hydraulic resistance of the fouling layer under elevated TMP during dead-end filtration, without correlating this to the physical structure of the fouling layer. Dreszer et al. (2013) also reported that biofilm hydraulic resistance increases at higher permeate fluxes. However, Dreszer et al. (2013) calculated the biofilm thickness based on biofilm weight per specific area, meaning that compression effects on biofilm morphology could not be detected.

Later developments of *in-situ* imaging techniques such as optical coherence tomography (OCT) enabled researchers to study biofilm development (Wagner et al., 2010; Wang et al., 2017) and structural deformation in real-time during compression (Blauert et al., 2015; Desmond et al., 2018c). Biofilm thickness and hydraulic resistance were correlated using *in-situ* OCT imaging techniques during MF process (Dreszer et al., 2014). It was observed that the biofilm hydraulic resistances increased at larger permeate fluxes and the resistance returned almost to its original value as compression forces were released. However, in the study of Dreszer et al. (2014) the severe changes in resistance were only accompanied by a slight change in biofilm thickness. Valladares Linares et al. (2015) also related the change in hydraulic resistance of MF biofouling to the biofilm thickness and structural deformation through OCT imaging. Furthermore, Derlon et al. (2016) measured increased biofilm hydraulic resistance with increasing TMP during a dead-end UF system. The correlation between biofilm resistance, biofilm thickness and biofilm roughness was later studied by Desmond et al. (2018c) in a gravity-driven membrane (GDM) system. They observed that the increase in hydraulic resistance is accompanied by a reduction of biofilm relative roughness (based on OCT images) during compression of several model biofilms. Interestingly, they also reported that the increase in hydraulic resistance of a river water biofilm could not be correlated to changes in biofilm thickness and roughness. Recently, Jafari et al. (2018) proposed a fluid-structural model that can explain the structural and hydrological responses of a smooth surface biofilm to compression during water filtration in membrane systems. The numerical model enabled the quantification of mechanical and hydrological properties of different biofilms.

The relation between structural deformation and hydraulic resistance during compression of biofilms with different morphologies (e.g., surface roughness) is not still clear. Therefore, this study aims at evaluating membrane biofilm compressibility and the corresponding changes in biofilm hydraulic resistance as a function of: i) biofilm growth conditions (i.e., growth time and growth TMP); ii) spatial distribution of mechanical and hydrological properties in the biofilm, and iii) biofilm surface roughness. To this goal, a computational model was developed and supported by experimental results.

2. Experimental set-up

2.1. Biofilm cultivation and growth conditions

Biofilms were cultivated in a flow cell under dead-end ultrafiltration mode with the membrane effective area of 18.75 cm^2. Biofilms developed from filtration of river water (Chriesbach river, Dübendorf, Switzerland) during winter, under growth conditions listed in Table 1. The detailed characteristics (Total organic carbon, dissolved organic carbon, assimilable organic carbon, etc.) of feed water used for biofilm growth can be found in (Derlon et al., 2013) and in supplementary information Table S1. In the first experiment, we evaluated the effect of biofilm age (20 and 30 days), when grown under constant transmembrane pressure (TMP = 0.06 bar). In the second experiment, the effect of TMP (0.06 and 0.28 bar) during biofilm growth was studied. To evaluate data reproducibility, biofilms were grown in several parallel flow cells in each growth condition.

2.2. Biofilm compression experiments

The biofilms grown in parallel flow cells were subjected to the compression/relaxation tests consisting of gradual increase/decrease of TMP to specific values, as defined in Fig. 1. Biofilms were subjected to an identical compression and relaxation cycle regardless of their growth TMP. The TMP range (between 0.06 and 0.5 bar) was selected based on practical implications and construction limitations GDM systems. Biofilms were discarded after one compression/relaxation test. All compression tests were done in a 20 °C temperature-controlled room.

2.3. Hydraulic parameters

The permeate flux in [$L/m^2/h$] was calculated from mass measurements of collected permeate. The biofilm hydraulic resistance R_{bio} [m^{-1}] resulted from the difference between the total hydraulic resistance R_{tot} and membrane resistance R_{mem}, as explained in Martin et al. (2014). The total filtration resistance was calculated through Darcy's law based on applied TMP and the measured permeate flux in the presence of biofilm (Jafari et al., 2018). The intrinsic membrane resistance, R_{mem}, was measured with nanopure water for 24 h prior to fouling.

2.4. Biofilm morphology quantification

The morphological response of biofilms to compression forces was determined by means of optical coherence tomography (OCT) (Ganymede GAN210, Thorlabs GmbH, Dachau, Germany), light source center wavelength of 930 nm and refractive index of 1.33. In order to improve statistical certainty of biofilm morphological properties, at least 10 images were taken at random locations in each flow cell, at each pressure step. Mean biofilm thickness and surface roughness were quantified using a customized MATLAB routine (MathWorks, Natick, US). Mean absolute surface roughness (δ_{abs}) shows biofilm thickness variability averaged for a number of image locations, according to eq. (1). Moreover, mean roughness coefficient (δ_{rough}) was calculated, which indicates biofilm thickness distribution normalized to mean biofilm thickness based on eq. (2) (Murga et al., 1995)

Table 1
Experimental conditions used in this study.

Experiment	Name	Growth time [days]	Growth TMP [bar]	Number of parallel flow cells
(1) Effect of growth time	*E1*	20	0.06	4
	E2	30		3
(2) Effect of growth TMP	*E2*	30	0.06	3
	E3		0.28	3

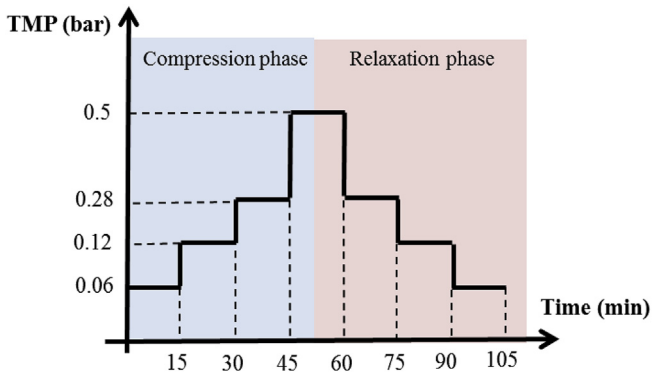

Fig. 1. Loads were applied on the biofilms by a step-wise change of TMP (compression/relaxation phases) in intervals of 15 min.

$$\delta_{abs} = \frac{1}{n}\sum_{i=1}^{n}\left|L_f - \overline{L_f}\right| \quad (1)$$

$$\delta_{rough} = \frac{1}{n}\sum_{i=1}^{n}\frac{\left|L_f - \overline{L_f}\right|}{\overline{L_f}} = \frac{\delta_{abs}}{\overline{L_f}} \quad (2)$$

where n is the number of measurements, L_f is biofilm local thickness and $\overline{L_f}$ is the mean biofilm thickness.

3. Model description

3.1. Model geometry and physics

The mathematical model used to correlate the biofilm structural deformation with the corresponding changes in hydraulic resistance during compression was presented in details in (Jafari et al., 2018), therefore the model is here only briefly described. In this poroelastic model, fluid flow in the biofilm was reciprocally coupled to the structural mechanics of the biofilm. The gradient of liquid pressure in biofilm pores affects the effective stress in the biofilm and leads to structural deformation, while the deformation changes the permeability and consequently the pore pressure.

Due to the dead-end filtration mode, the biofilm properties would change mainly in the direction of permeate flow (i.e., perpendicular to the membrane). However, a two-dimensional (2-D) model was developed to evaluate the effect of biofilm surface roughness on permeate flux and biofilm deformation (Fig. 2). Two different geometries were used to represent both smooth (cases 1 and 2) and rough surface biofilms (cases 3 to 6 in Table 2). Average biofilm thickness (L_f) and biofilm length (L_x) of the model biofilms were based on experimental results. The membrane was represented by an additional layer with thickness, L_m. The biofilm base layer thickness L_b and top layer thickness L_t in the bi-layer model biofilm were constructed so that the sum ($L_b + L_t$) equals the average thickness (L_f). In case of smooth-surface biofilm (cases 1 and 2) the model could in principle be reduced to one-dimension (Jafari et al., 2018), however, for consistency, we kept the 2-D model geometry for all six cases. Finally, the biofilm depth in the third dimension (z) was considered to be large enough to apply the 2-D plane-strain simplification (Coussy, 2004).

The velocity and pressure fields for water flow through the biofilm were calculated from Darcy's law, with permeability K being related to biofilm porosity φ by a linear relationship $K = A\varphi$ in which A *is* the biofilm permeability coefficient. Under compression, local biofilm porosity $\varphi(x,y)$ is related to the porosity prior to compression, φ_0, and biofilm displacement gradient in the compression direction (i.e., local strain in y-direction, ε_y) through equation (3) (MacMinn et al., 2016)

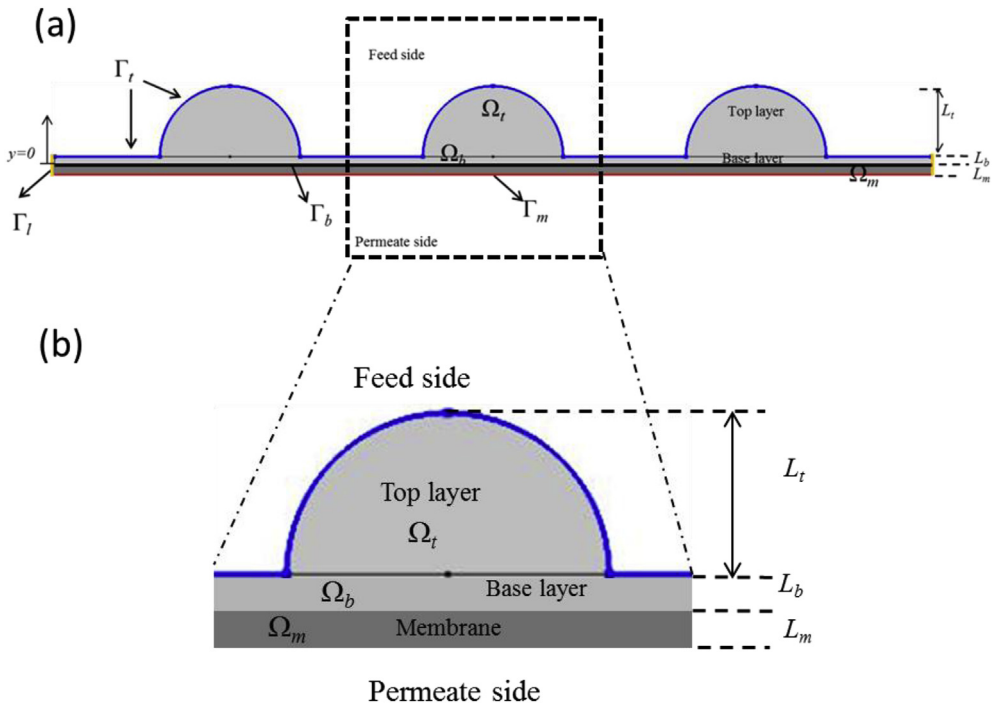

Fig. 2. General model geometry for rough-surface biofilm. Ω_t: top layer domain; Ω_b: base layer domain and Ω_m: membrane domain (not represented at scale here). Liquid flow was calculated in all the domains while structural mechanics was applied only to Ω_b and Ω_t domains. Γ_t: top layer boundary was set to constant pressure (0.5 bar); Γ_b: base layer boundary conditions were set to zero deformation; Γ_m: permeate side subjected to zero relative pressure so that the TMP matched the value used in the experiment and Γ_l: symmetry conditions were applied to the lateral boundaries. The zoomed geometry shows part of the model geometry including one cluster with different domains.

Table 2
Biofilm geometries and specifications of six case study biofilms.

Case No.	Case 1	Case 2	Case 3
Name	1-F	2-*F*-(E, φ)	1-R
Model geometry			
Specifications	E = Const. φ = Const.	$E_b > E_t$ $\varphi_b < \varphi_t$	E = Const. φ = Const.
Case (cont.) Name (cont.)	Case 4 2-*R*-φ	Case 5 2-*R*-*E*	Case 6 2-*R*-(E, φ)
Model geometry			
Specifications	E = Const. $\varphi_b < \varphi_t$	$E_b > E_t$ φ = Const.	$E_b > E_t$ $\varphi_b < \varphi_t$

$$\frac{\delta d_y}{\delta y} = \varepsilon_y = \frac{\varphi - \varphi_0}{1 - \varphi_0} \tag{3}$$

The biofilm displacement tensor **d** resulted from the balance of momentum for a saturated porous material (Biot poroelasticity (Coussy, 2004),). The linear elastic response depends on the elastic modulus E and Poisson's ratio ν of the biofilm. In case of bilayer biofilms, different hydraulic and/or mechanical properties were applied in each layer. Applied boundary conditions are presented in Fig. 2 and all model parameters are in Table 3.

3.2. Model cases and their structure

Six biofilm cases were selected based on their morphology (rough or smooth surfaces) and structures (mono-layer or bi-layer). Biofilms have different surface roughness properties and multi-layer structure depending on their growth conditions, as reported by Desmond et al. (2018c). They also observed during dead-end filtration that biofilms developed under phosphate limitation had smooth surface and mono-layer structure as opposed of river water biofilms that had rough surface and bi-layer structure (Desmond et al., 2018b). Existence of base layer can be explained by biofilm stratification (densification) adjacent to the substratum (e.g., membrane) caused by different growth condition parameters such as hydrodynamic strengths, carbon sources, organic loading rate and culture time (Bishop et al., 1995; Derlon et al., 2008; Okabe et al., 1996). In addition, biofilm porosity and elastic modulus were selected as distinctive properties in determination of biofilm hydraulic and mechanical behaviour (Jafari et al., 2018). Thus, in this study we selected smooth surface (case 1 and 2) and rough surface biofilms (case 3 to 6). To evaluate the importance of the bi-layer structure, four biofilm cases with different porosity and/or elastic modulus among the layers were set up (cases 2, 4, 5 and 6). Table 2 shows biofilm morphologies and specifications of the six chosen cases.

3.3. Model solution

The 2-D fluid-structure interaction model was solved in COMSOL Multiphysics (v5.3.a, COMSOL Inc., Burlington, MA). The fluid flow in porous media was coupled with plane strain structural mechanics and computed through a stationary solver. Triangular mesh elements had a maximum size of 2 μm, to ensure the solution independency on mesh size.

4. Results

4.1. Correlation between biofilm hydraulic resistance and the structural deformation

River water biofilms were cultivated in parallel flow cells, under three different conditions. Fig. 3 shows the biofilm mean thickness and hydraulic resistance measured during a compression and relaxation cycle. As expected, biofilms grown for longer time (30 days) were thicker (70 ± 10 μm, average thickness) than younger biofilms (40 ± 3 μm after 20 days), under the same growth TMP (0.06 bar) (Fig. 3a and b). Furthermore, biofilms grown under high TMP (0.28 bar) were thinner (50 ± 3 μm, average thickness)

Table 3
Model parameters for biofilm grown 20 days under TMP = 0.06 bar.

Parameter	Symbol	River water biofilm	Unit	Source
Biofilm length	L_x	1000	μm	Experimental[c]
Average biofilm thickness before compression (initial)	L_f	~40	μm	Experimental[c]
Initial top biofilm layer	L_t	80	μm	Experimental[c]
Initial base biofilm layer	L_b	10	μm	Experimental[c]
Membrane thickness	L_m	200	μm	Experimental
Membrane resistance	R_m	4×10^{11}	m^{-1}	Experimental
Biofilm permeability coefficient	A	1×10^{-17}	m^2	Fitted
Initial top layer porosity	φ_{t0} ($= \varphi_0$)[b]	0.8	–	Chosen
Initial bottom layer porosity[a]	φ_{b0}	0.5	–	Chosen
Elastic modulus of top layer	E_t ($= E$) [b]	5	kPa	Fitted
Elastic modulus of base layer[a]	E_b	7.5	kPa	Fitted
Poisson's ratio	ν	0.48	–	Kundukad et al. (2016)

[a] Values used in applicable cases.
[b] Values for top layer were used in the cases with constant properties.
[c] Based on OCT images of the specified biofilm.

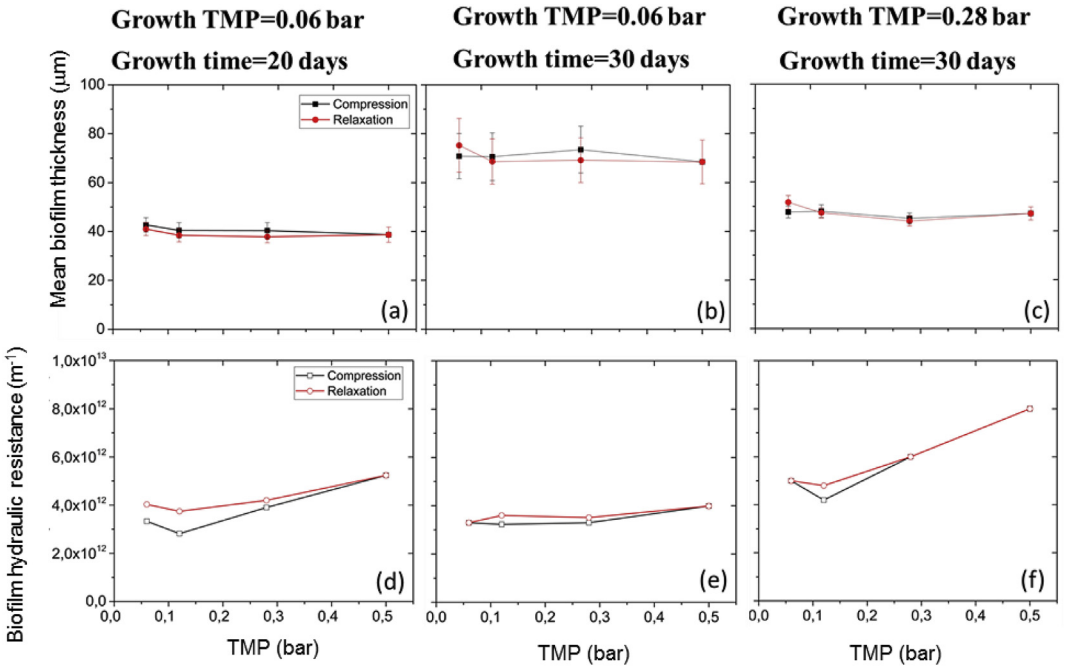

Fig. 3. Change in mean biofilm thickness (a–c) and hydraulic resistance (d–f) of river water biofilms during compression/relaxation tests. Biofilms were grown in three conditions: (a,d) TMP = 0.06 bar for 20 days, (b,e) TMP = 0.06 bar for 30 days, (c,f) TMP = 0.28 bar for 20 days. Biofilm thickness was calculated based on minimum of 10 images taken at random locations. See Supplementary Information Fig. S2 for mean biofilm thickness and hydraulic resistance in other parallel flow cells, showing similar trends.

compared to the low TMP (0.06 bar) biofilms, at the same age (30 days) (Fig. 3b and c). Interestingly, when subjected to compression and relaxation phases, the river water biofilms did not undergo a significant structural deformation (i.e., change in thickness and roughness) (Fig. 3a–c). A relatively constant biofilm thickness is also observed in the time-lapse videos in Supplementary Information, **SI-V1** and **SI-V2**, while the membrane displacement clearly indicates the applied pressure steps. However, biofilm hydraulic resistance increases significantly during compression over TMP range of 0.06–0.5 bar (Fig. 3d–f): from 3×10^{12} to 5×10^{12} m^{-1} for the biofilm grown at 0.06 bar for 20 days and from 3×10^{12} to 4×10^{12} m^{-1} for the biofilm developed for 30 days. Biofilms grown under high TMP (0.28 bar) showed greater hydraulic resistance change from 5×10^{12} to 8×10^{12} m^{-1} during compression tests. These measurements clearly confirm that biofilms grown under higher TMP were more compact (thinner) (Fig. 3b and c) and associated higher hydraulic resistance (Fig. 3e and f).

4.2. Effect of growth conditions on biofilm surface morphology

Experiments in UF flow cells have shown that the growth conditions affect not only the biofilm thickness, but also the biofilm surface roughness. Fig. 4 displays biofilm surface morphology properties (i.e., mean absolute roughness and mean relative roughness coefficient) developed in different conditions. Clearly, the biofilms after 30 days of cultivation showed higher roughness coefficient ($\delta_{rough} = 0.3 \pm 0.05$) than after 20 days ($\delta_{rough} = 0.16 \pm 0.05$) when grown under TMP = 0.06 bar (Fig. 4a). Moreover, the biofilms grown at larger pressure were smoother ($\delta_{rough} = 0.11 \pm 0.05$) compared to biofilms grown at low pressures (Fig. 4a). Similar trend was observed in biofilm mean absolute roughness (Fig. 4b). However, change in the biofilm roughness measured during compression of river water biofilms did not follow any clear trend (as also reported in other studies, e.g. Desmond et al. (2018c)).

4.3. Selection of a fluid-structure biofilm model correlating thickness and resistance under compression

Experimental measurements of river water biofilms under compression showed a considerable increase in hydraulic resistance (up to ~ 60%), while biofilm thickness only slightly changed. To explain the correlation between biofilm thickness and resistance during compression, we developed a fluid-structural model and evaluated several biofilm possible structures with different morphological, mechanical and hydrological properties (Table 2). Three main variables (mean biofilm displacement, change in hydraulic resistance and water flux) were calculated and compared with experimental results of biofilm grown for 20 days under TMP = 0.06 bar (Fig. 5). The fitting parameters (Table 3) were selected for each model biofilm individually, so that the three measured variables are optimally represented.

The model results of mean biofilm displacement obtained by *one-layer-rough* (case 3), *dual-porosity-rough* (case 4) and *dual-porosity-elasticity-rough* biofilm models (case 6) are in agreement with experimental results. However, the mean displacement in other model cases was still within range of experimental results (Fig. 5a). Furthermore, the measured water flux was around 20–35 L/m^2/h, which is compatible with the calculated flux for *one-layer-flat* (case 1), *dual-porosity-elasticity-flat* (case 2), *dual-porosity-rough* (case 4) and *dual-porosity-elasticity-rough* biofilm models (case 6), Fig. 5b**.** Finally**,** Fig. 5c indicates that *dual-porosity-elasticity-flat* (case 2), *dual-porosity-rough* (case 4) and *dual-porosity-elasticity-rough* (case 6) biofilm models could explain a significant increase in hydraulic resistance (40–60%) during compression. Considering all three criteria, the dual-layer rough biofilms (Cases 4 and 6) are the most suitable to explain the experimental results. The difference between cases 4 (constant mechanical properties across the biofilm) and 6 (layers of different elasticity) shows that a gradient of initial biofilm porosity is more important than a gradient of mechanical properties in determination of biofilm deformation and hydraulic resistance during

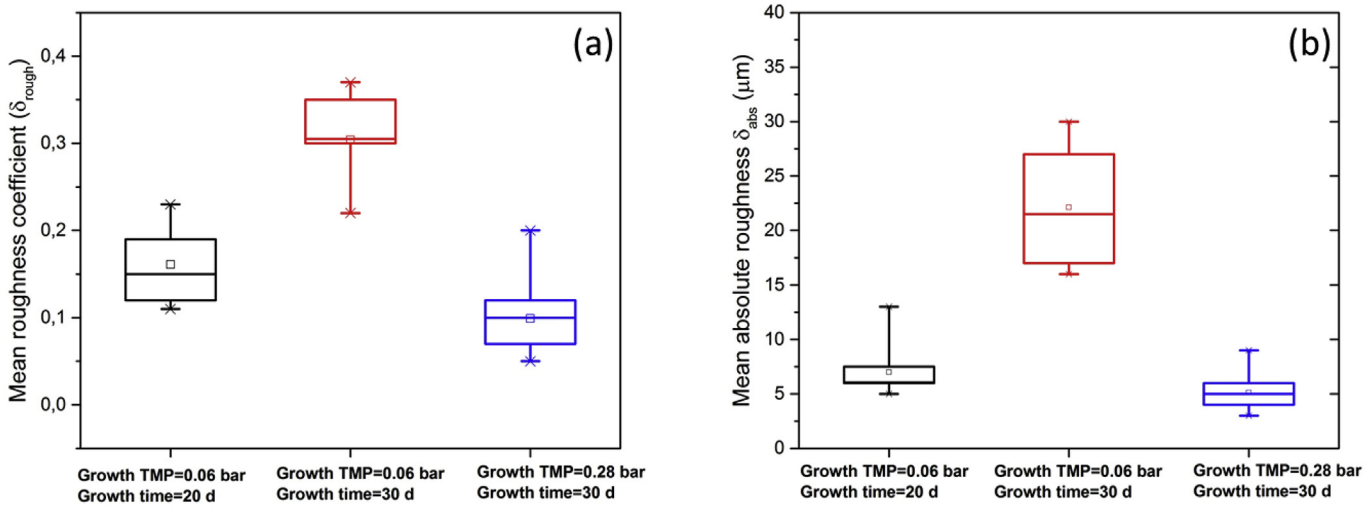

Fig. 4. Effect of cultivation TMP (0.06 and 0.28 bar) and biofilm age (20 and 30 days) on the biofilm roughness properties. (a) Mean roughness coefficient and (b) mean absolute roughness, both increase with cultivation time and decrease with cultivation TMP. Results represent deviations for minimum 10 images taken at different locations in the same flow cell.

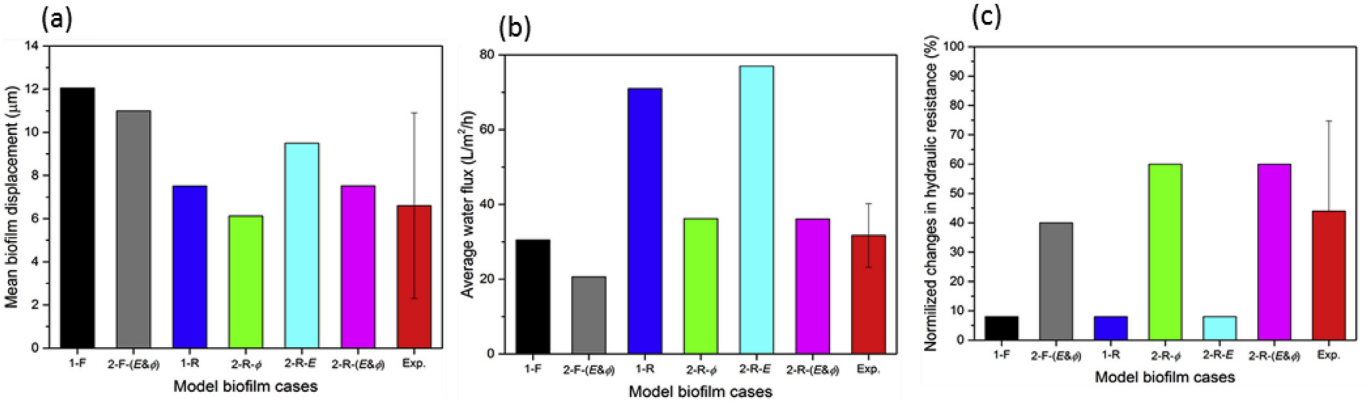

Fig. 5. Comparison between the six different models and experimental results of biofilm grown 20 days under TMP = 0.06 bar and compressed under TMP = 0.5 bar in dead-end UF. (a) biofilm mean displacement, (b) water flux and (c) changes in biofilm hydraulic resistance, normalized to the initial membrane resistance.

compression. Therefore, case 4 (*dual-porosity-rough*) was selected to further evaluate biofilm local properties during compression, due less model parameters required compared with case 6.

4.4. Model calibration and parameters estimation

All the model cases were calibrated with experimental results of biofilms grown for 20 days under TMP = 0.06 bar. Model parameters used in this study are shown in Table 3. Geometric parameters (i.e., biofilm average thickness, base and top layers thickness and top layer coverage area) were selected based on OCT images and biofilm morphological properties of the specific biofilm. Initial porosity of top and base layers (if applicable) were chosen with the assumption that porosity of base layer is lower than top layer porosity prior to compression (Gao et al., 2011b). The porosity values and distribution in biofilms were in accordance with the observations reported by (Blauert et al., 2015; Gao et al., 2011b; Wagner et al., 2010). In the model calibration procedure, initial biofilm porosity of both layers (if applicable) was kept constant and only fitting parameters (permeability coefficient, elastic modulus) were changed to calibrate the models. Moreover, during model selection procedure (Fig. 5), a model was considered acceptable only if the model results were within the range of experimental data (considering experimental deviations). For example, in Fig. 5a all the models were acceptable for biofilm deformation due to the large spreading of data in the experiments. Sensitivity analysis of the proposed fluid-structure model to different parameters has been presented in our previous work (Jafari et al., 2018).

4.5. Local biofilm properties during compression

Computed 2-D distributions of the main model variables during compression (TMP = 0.5 bar) are presented in Fig. 6. The water flows at higher velocity through the thin biofilm sections (~14 μm/s), while the water velocity in the thicker parts (i.e., top layer) is much lower (~2 μm/s) (Fig. 6a). As expected, lower biofilm thickness results in lower hydraulic resistance and higher fluxes. The biofilm experiences the highest stress (2500 N/m^2, Von Mises stress) near the membrane, compared to the top layer (570 N/m^2), as shown in Fig. 6b. In addition, due to large pressure drop, the stress is higher in the thick biofilm parts. Considering the relation of stress and strain, thus, greater local strain is observed in the biofilm next to the membrane (Fig. 6c). The top biofilm layer displaces more (13 μm) than the base layer (1 μm), due to the cumulative effect of strain on displacement (Fig. 6d). Higher local strain leads to lower biofilm porosity (Fig. 6e) based on eq. (3) and, consequently,

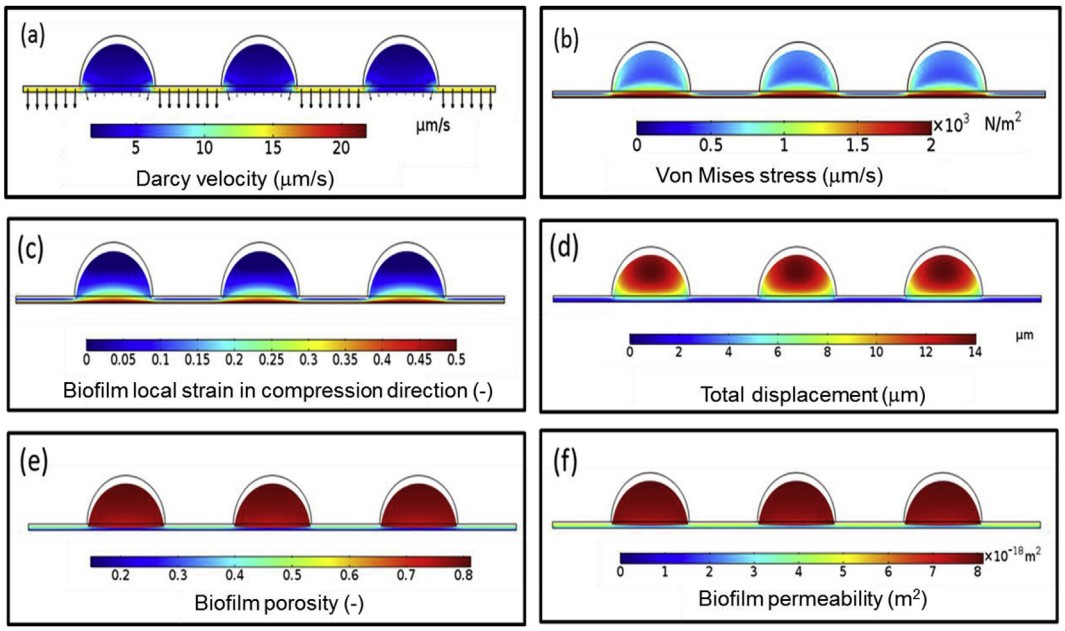

Fig. 6. Calculated biofilm local variables after compression. (a) water velocity magnitude and direction in biofilm and membrane; (b) Von Mises stress developed in the biofilm; (c) biofilm strain in compression direction; (d) total biofilm displacement; (e) biofilm porosity; (f) biofilm permeability. Results are based on *dual-porosity-rough* model (Case 4), with parameters determined for the biofilm grown 20 days under TMP = 0.06 bar and compressed under TMP = 0.5 bar. Membrane domain is not shown.

to reduced permeability (Fig. 6f). Although the biofilm top layer porosity remains almost constant ($\varphi = 0.8$), the base layer undergoes a significant reduction of porosity after compression ($\varphi = 0.3$ to 0.15). Similarly, biofilm permeability in top layer remained around 14×10^{-18} m^2 after compression, while the permeability decreased to ~1×10^{-18} m^2 in the base layer.

Spatial distributions of biofilm porosity, permeability and physical structure (i.e., thickness) along the membrane surface cause heterogeneity of water flux along the membrane. Fig. 7a shows a pronounced difference in the calculated water flux at the biofilm base along the flow cell (~15–50 L/m^2/h), whereas the flux is homogenized by flow through the membrane (37–41 L/m^2/h). This considerable difference in flux distribution between biofilm and membrane boundaries (Fig. 7a) is correlated to flux homogenization in membrane domain, caused by lower membrane resistance and greater thickness compared to the biofilm).

A more detailed analysis demonstrates that due to distinct biofilm properties in the top and base layers, porosity and permeability undergo different behaviors during compression. Fig. 7b shows biofilm strain in the compression direction, ε_y, across the biofilm depth, after compression at TMP = 0.5 bar. The strain decreases from 0.7 at the membrane side to zero at the liquid side. The small change in strain gradient at the base layer/top layer interface is caused by the difference in porosity of the two layers. Fig. 7c demonstrates that the top layer porosity remains almost constant after compression, while biofilm porosity in base layer drastically decreases from its initial value (0.5) to 0.3 in top of base layer and 0.15 at the membrane surface.

4.6. Evaluation of flux and deformation from OCT biofilm images

Exact biofilm surface geometries (initial and after compression) were extracted from OCT images and the water flux and biofilm deformation were calculated on these geometries using the *dual-porosity-rough model* (case 4). Fig. 8a and b shows OCT images of the biofilm under transmembrane pressure of 0.06 and 0.5 bar, respectively. Fig. 8a and b demonstrate that the biofilm underwent a very small deformation during compression (max. 10 μm at the top), while a significant change in hydraulic resistance was observed. Coupling of OCT images with the fluid-structural model allows for the computation of water flux and biofilm deformation under compression on the exact biofilm geometries. Negligible biofilm deformation was calculated under compression, in accordance with OCT results: red line in Fig. 8c shows biofilm surface under compression of 0.5 bar.

4.7. Effect of biofilm surface morphology on flux and deformation during compression

4.7.1. Biofilm roughness (effect of cluster height)

The numerical model developed for the Case 4 (*dual-porosity-rough biofilm*) was also used to evaluate the effect of biofilm surface roughness on the hydraulics and structural response of the biofilm to the same compression conditions (TMP = 0.5 bar). To ensure that the area of base layer in contact with the liquid remained constant, the roughness was increased by changing the half-circular colonies into half-ellipses with increasing semi-major axes (four structures, shown in Fig. 9a).

Increasing the biofilm surface roughness from 20 to 80 μm (i.e., peaks 50–200 μm high) resulted in a total deformation from 8 to 13 μm, respectively. Fig. 9b shows that the total biofilm average displacement is mainly determined by the top layer (displaced 10–16 μm), while the base layer is less compressed (4 μm). However, more biofilm surface roughness just slightly decreases water flux during compression, from 34 L/m^2/h ($\delta_{abs} = 20$ μm) to 32 L/m^2/h ($\delta_{abs} = 80$ μm). Water flux approached a constant value as the surface roughness increased above 35 μm, which implies that the contribution of top sections to the water flux becomes negligible at high roughness.

4.7.2. Fraction of exposed base layer

Since the biofilm roughness does not significantly impact the permeate flux accordingly to our model results, we also evaluated other potential morphological parameters. The permeate flux

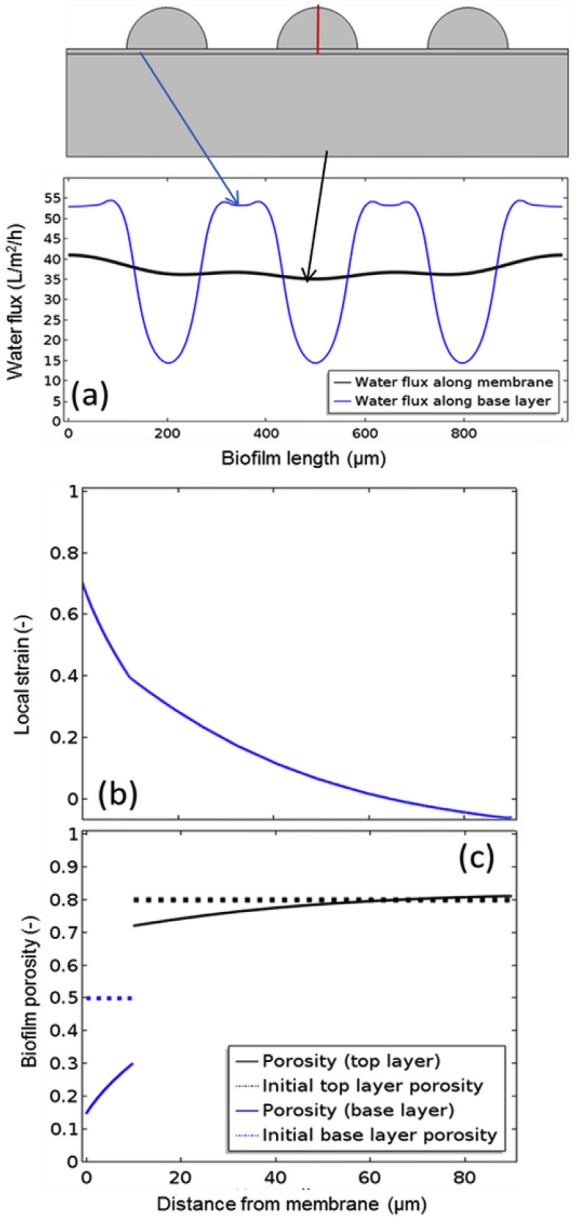

Fig. 7. (a) Local permeate flux along the biofilm base (blue line) and permeate side of the membrane (thick black line); (b) Strain in the compression direction in base and top biofilm layers, along the cut line shown in red in (a); (c) Biofilm porosity in base and top layers, along the same cut line. Dotted lines show initial values and solid lines values after compression. Arrows demonstrated the boundaries which water fluxes were computed. Simulation conditions as in Fig. 6. (For interpretation of the references to color in this figure legend, the reader is referred to the Web version of this article.)

during compression was calculated for three biofilm geometries with different morphologies (Table 4). Biofilm geometries were selected in which have identical average thickness and roughness values, but different fractions of base layer exposed to bulk liquid. To satisfy the mentioned criteria, different top/base layers thickness values were chosen. Fraction of exposed base layer was defined as area of biofilm base layer divided by the total biofilm surface area. The *dual-porosity-rough model* (Case 4) was applied and permeate fluxes were calculated under TMP = 0.5 bar. Model results clearly demonstrate that configurations with higher fraction of exposed base layer (i.e., 0.71 for config. II) allow higher water flux (27.4 L/m^2/h) compared to 10 and 20.7 L/m^2/h for config. I and config. III, respectively (Table 4).

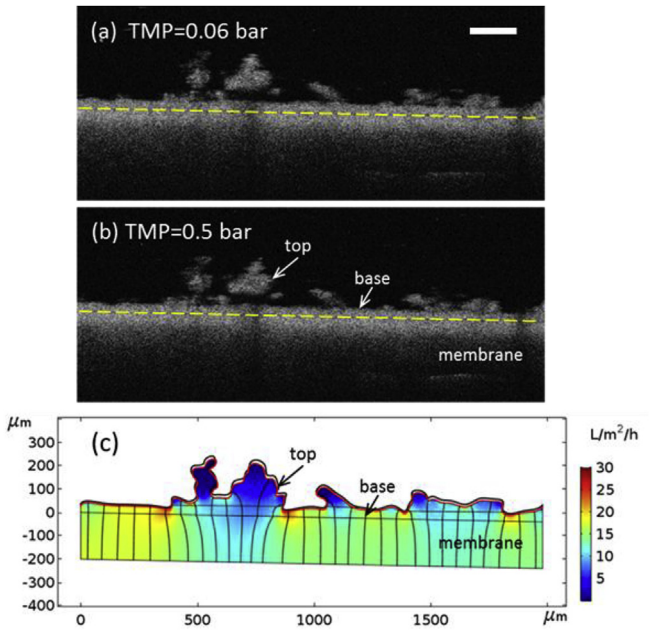

Fig. 8. (a),(b) OCT images of biofilm structure at TMP = 0.06 and 0.5 bar, respectively. The biofilm was grown under TMP = 0.06 bar for 30 days. The yellow dashed line represents the membrane/biofilm interface. Scale bar: 200 μm. (c) Computed water flux (colored surface) and streamlines (black lines), using the *dual-porosity-rough model* (case 4). Black thick line: biofilm surface at 0.06 bar; Red thick line: biofilm surface under compression at 0.5 bar. (For interpretation of the references to color in this figure legend, the reader is referred to the Web version of this article.)

5. Discussion

Biofilm hydraulic resistance and structural deformation. Biofilms grown under high TMP showed higher hydraulic resistance and lower thickness compared to biofilms developed under low TMP (Fig. 3). In addition, biofilms grown under high TMP showed lower roughness values compared to biofilm developed under low TMP (identical growth time) (Fig. 4). This could be explained by higher drag force (induced by higher flux) and consolidation effect caused by the long-term continuous compression under high TMP. These results agree with other reported observations (Casey, 2007; Derlon et al., 2016; León Ohl et al., 2004). Biofilms developed under high TMP are likely more compact (i.e., lower porosity), which reduces the biofilm permeability and ultimately increases its hydraulic resistance. In this study we consistently observed that the increase in biofilm hydraulic resistance during compression was accompanied by limited biofilm deformation (Fig. 3 and **Supplementary Information, SI-V1 to SI-V2**). A similar trend was also reported previously (Desmond et al., 2018a; Dreszer et al., 2014). One possible explanation for the increased hydraulic resistance would be a reorganization of the biofilm material (McCarthy et al., 2002) at a scale lower than the OCT resolution (thus not observable by OCT), while the biofilm thickness remains approximatively constant. Other authors related the larger hydraulic resistance during compression to the collapse of the mushroom-like biofilm structure (Valladares Linares et al., 2015) and the corresponding loss in macro-porosity (Fortunato et al., 2017), with a significant reduction in biofilm thickness. In our study, due to the small measured deformation during compression, we propose that the hydraulic resistance increase was caused by pore/particle reorganization at a scale lower than the OCT detectable threshold. In addition, simulation results confirm that in case of the base layer deformation equal to OCT detectable threshold (~3 μm), biofilm hydraulic resistance would rise by 110%, in agreement with the observed

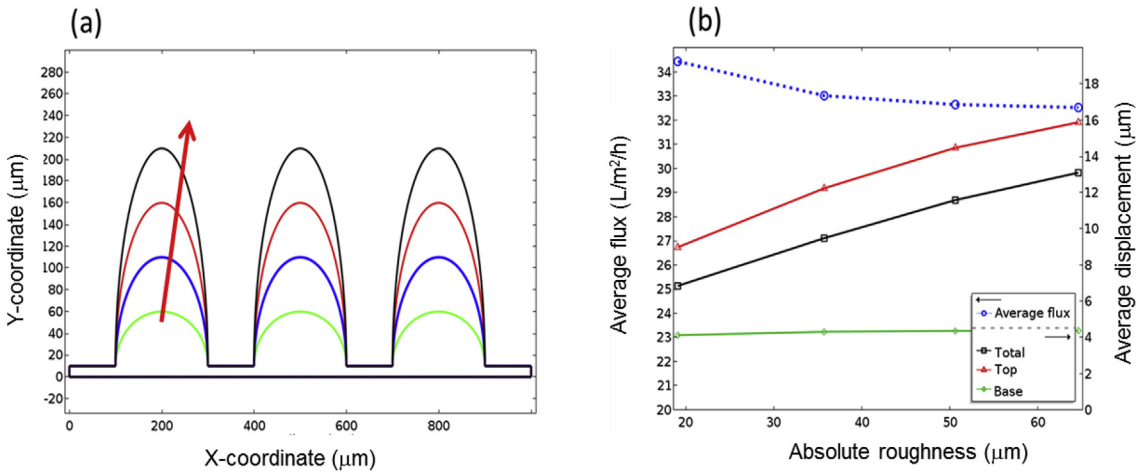

Fig. 9. (a) Biofilm geometries used to evaluate effect of morphology (arrow shows increased surface roughness) on water flux and biofilm deformation during compression; (b) average water permeate flux and average displacement of different sections of the biofilm. Simulation conditions as in Fig. 6.

Table 4
Three model biofilm configurations (geometries) with similar morphological properties (average thickness and surface roughness). Biofilms with greater fraction of exposed base layer lead to higher permeate flux. Results are based on *dual-porosity-rough model* (Case 4 parameters) and compression under TMP = 0.5 bar.

Configuration	Model configuration	OCT image	Average thickness	Roughness coefficient	Absolute roughness	Fraction of exposed base layer	Water flux (L/m²/h)
Config. I		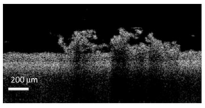	~53 (μm)	0.48	~25 (μm)	0.2	14
Config. II		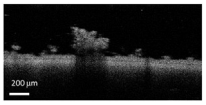	~53 (μm)	0.48	~25 (μm)	0.71	27.4
Config. III		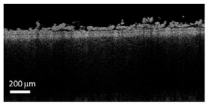	~53 (μm)	0.48	~25 (μm)	0.33	20.7

results.

The biofilm model selection. A bi-layer morphology with a porous layer on top of a thin and dense base layer was observed by Derlon et al. (2016) and Desmond et al. (2018b) for biofilms developed under dead-end GDM. In order to explain the observed trend in biofilm structural deformation and the corresponding hydraulic resistance, several biofilm models were evaluated. The poroelastic numerical model proposed in Jafari et al. (2018) for smooth surface biofilms was extended here to include rough surface with dual-layer properties. Fig. 5 confirms that only cases 4 and 6 (i.e., rough and double-layer biofilm, as observed in experimental results from Fig. 5) could explain the small total biofilm deformation associated with significant rise of hydraulic resistance under compression.

The gradient of porosity across the biofilm is more important than the gradient of elastic modulus for fluid-structural models. Gradients in biofilm porosity (Blauert et al., 2015; Okabe et al., 1998; Zhang and Bishop, 1994) or biofouling layer porosity (Gao et al., 2011a) were reported, with generally a dense base layer and more porous top layer. In this study, both model cases 4 and 6 can explain the observed trends in biofilm compressibility (Fig. 5). However, the model case 4 (i.e., same elastic modulus across both layers) would be preferable as it contains less parameters and thus it is simpler (Table 2). The comparison between model cases shows that the biofilm deformation is mainly a result of pore compression, and the variable mechanical properties can be achieved by a gradient in porosity. This observation can further be used to simplify development of fluid-structure models. However, one should note that when water is not forced through the biofilm (e.g., biofilm developed on pipe walls) a gradient in elastic modulus could be important for the mechanical response (as permeate flux and porosity are not relevant) (Picioreanu et al., 2018).

Biofilm local properties. Water permeates mostly through the thin parts of the biofilm due to lower hydraulic resistance (Figs. 6a, 7a and 8). This is in accordance with the computations by Martin et al. (2014) for model biofilm in GDM. Fortunato et al. (2017) reported unusual calculation results in which the permeate flux through biofilm peaks is larger than the flux through the thinner parts (biofilm cavities), in a submerged membrane biofilm reactor. They claimed this observation is due to the effect of liquid vortices in biofilm cavities leading to lower pressure gradient. However, their result is physically unrealistic because small axial velocities would only lead to negligible pressure drop compared to the trans-membrane pressure gradient.

During compression, the biofilm porosity decreases mainly in the base layer (near the membrane) (Figs. 6e and 7c), which is in

agreement with reported results by MacMinn et al. (2016) and Radu et al. (2015) for soft porous materials under deformation. Thus, during compression of the fouling layer, the base layer permeability decreases much more than in the top layer (due to local porosity reduction). Therefore, the base layer becomes even more important in the determination of water flux. However, not all biofilms may display this bi-layered structure. Desmond et al. (2018b) observed that for biofilms with smooth surface (i.e., synthetic biofilm developed under phosphate-limiting conditions), biofilm hydraulic resistance is determined by the whole biofilm structure and not by a dense base layer.

Effect of biofilm surface roughness on permeate flux. Although biofilm surface roughness affected the structural response during compression, its impact on the total permeate flux was not significant (Fig. 9). Again, this could be explained by the fact that the magnitude of the permeate flux is mainly dictated by the base layer. Derlon et al. (2012) reported that predation by eukaryotic microorganisms leads to heterogeneous biofilm structure with larger surface roughness accompanied by lower membrane coverage. The reduced membrane coverage caused higher values of the measured permeate flux at greater biofilm surface roughness.

Fraction of exposed base layer. Although biofilm surface properties, such as roughness coefficient and thickness, are generally useful when characterizing biofilm morphology (Li et al., 2016; Zhang et al., 1994), these measures are not adequate when water flux is concerned. Biofilms with identical roughness and thickness might lead to different water fluxes during compression (Table 4). Fraction of exposed base layer proves to be a better indicator to correlate permeate flux and biofilm surface morphology in membrane systems. A greater fraction of exposed base layer would result in a higher permeate flux through the biofilm.

6. Conclusions

- An increased biofilm hydraulic resistance during compression is not necessarily accompanied by large structural deformation (i.e., not observable by OCT). The rise in resistance could be explained by micro-scale particle/pore reorganization of biofilms under pressure;
- Hydraulic resistance of membrane biofilm formed from river water is mainly governed by properties of their base layer (i.e., density, porosity and fraction of base layer exposed to bulk liquid), while deformation is governed by biofilm roughness;
- A poroelastic fluid-structural model was proposed to explain various biofilm behaviors under compression. The dual-layer biofilm with a porous top layer and a dense base layer can explain the observed increase in hydraulic resistance coupled with minor structural deformation;
- Model simulations indicate that, when developing fluid-structural models for membrane systems, considering a gradient in biofilm initial porosity is more important than a gradient in the elastic modulus. This allows to reduce complexity of poroelastic models;
- Biofilm surface roughness alone does not impact significantly water permeate flux under compression. The fraction of exposed base layer could be a better biofilm morphology indicator in determination of permeate flux.

Declaration of interests

The authors declare that they have no known competing financial interests or personal relationships that could have appeared to influence the work reported in this paper.

Acknowledgements

This study was funded by European Union's Horizon 2020 research and innovation programme under the Marie Skłodowska-Curie grant agreement No. 676070 and the Swiss National Science Foundation BIOMEMBRA project, grant No. 149648. This communication reflects only the authors' view and the Research Executive Agency of the EU is not responsible for any use that may be made of the information it contains.

Appendix A. Supplementary data

Supplementary data to this article can be found online at https://doi.org/10.1016/j.watres.2019.03.073.

References

Aravas, N., Laspidou, C.S., 2008. On the calculation of the elastic modulus of a biofilm streamer. Biotechnol. Bioeng. 101 (1), 196–200.
Bishop, P.L., Zhang, T.C., Fu, Y.-C., 1995. Effects of biofilm structure, microbial distributions and mass transport on biodegradation processes. Water Sci. Technol. 31 (1), 143–152.
Blauert, F., Horn, H., Wagner, M., 2015. Time-resolved biofilm deformation measurements using optical coherence tomography. Biotechnol. Bioeng. 112 (9), 1893–1905.
Casey, E., 2007. Tracer measurements reveal experimental evidence of biofilm consolidation. Biotechnol. Bioeng. 98 (4), 913–918.
Coussy, O., 2004. Poromechanics. Wiley, UK.
Derlon, N., Grutter, A., Brandenberger, F., Sutter, A., Kuhlicke, U., Neu, T.R., Morgenroth, E., 2016. The composition and compression of biofilms developed on ultrafiltration membranes determine hydraulic biofilm resistance. Water Res. 102, 63–72.
Derlon, N., Koch, N., Eugster, B., Posch, T., Pernthaler, J., Pronk, W., Morgenroth, E., 2013. Activity of metazoa governs biofilm structure formation and enhances permeate flux during Gravity-Driven Membrane (GDM) filtration. Water Res. 47 (6), 2085–2095.
Derlon, N., Massé, A., Escudié, R., Bernet, N., Paul, E., 2008. Stratification in the cohesion of biofilms grown under various environmental conditions. Water Res. 42 (8), 2102–2110.
Derlon, N., Mimoso, J., Klein, T., Koetzsch, S., Morgenroth, E., 2014. Presence of biofilms on ultrafiltration membrane surfaces increases the quality of permeate produced during ultra-low pressure gravity-driven membrane filtration. Water Res. 60, 164–173.
Derlon, N., Peter-Varbanets, M., Scheidegger, A., Pronk, W., Morgenroth, E., 2012. Predation influences the structure of biofilm developed on ultrafiltration membranes. Water Res. 46 (10), 3323–3333.
Desmond, P., Best, J.P., Morgenroth, E., Derlon, N., 2018a. Linking composition of extracellular polymeric substances (EPS) to the physical structure and hydraulic resistance of membrane biofilms. Water Res. 132, 211–221.
Desmond, P., Böni, L., Fischer, P., Morgenroth, E., Derlon, N., 2018b. Stratification in the physical structure and cohesion of membrane biofilms — implications for hydraulic resistance. J. Membr. Sci. 564, 897–904.
Desmond, P., Morgenroth, E., Derlon, N., 2018c. Physical structure determines compression of membrane biofilms during Gravity Driven Membrane (GDM) ultrafiltration. Water Res. 143, 539–549.
Dreszer, C., Vrouwenvelder, J.S., Paulitsch-Fuchs, A.H., Zwijnenburg, A., Kruithof, J.C., Flemming, H.C., 2013. Hydraulic resistance of biofilms. J. Membr. Sci. 429, 436–447.
Dreszer, C., Wexler, A.D., Drusova, S., Overdijk, T., Zwijnenburg, A., Flemming, H.C., Kruithof, J.C., Vrouwenvelder, J.S., 2014. In-situ biofilm characterization in membrane systems using Optical Coherence Tomography: formation, structure, detachment and impact of flux change. Water Res. 67, 243–254.
Fortunato, L., Qamar, A., Wang, Y., Jeong, S., Leiknes, T., 2017. In-situ assessment of biofilm formation in submerged membrane system using optical coherence tomography and computational fluid dynamics. J. Membr. Sci. 521, 84–94.
Gao, W., Liang, H., Ma, J., Han, M., Chen, Z.-l., Han, Z.-s., Li, G.-b., 2011a. Membrane fouling control in ultrafiltration technology for drinking water production: a review. Desalination 272 (1), 1–8.
Gao, W.J., Lin, H.J., Leung, K.T., Schraft, H., Liao, B.Q., 2011b. Structure of cake layer in a submerged anaerobic membrane bioreactor. J. Membr. Sci. 374 (1–2), 110–120.
Herzberg, M., Kang, S., Elimelech, M., 2009. Role of extracellular polymeric substances (EPS) in biofouling of reverse osmosis membranes. Environ. Sci. Technol. 43 (12), 4393–4398.
Jafari, M., Desmond, P., van Loosdrecht, M.C.M., Derlon, N., Morgenroth, E., Picioreanu, C., 2018. Effect of biofilm structural deformation on hydraulic resistance during ultrafiltration: a numerical and experimental study. Water Res. 145, 375–387.
Jorgensen, M.K., Bugge, T.V., Larsen, P., Nielsen, P.H., Christensen, M.L., 2017. Membrane filtration device for studying compression of fouling layers in

membrane bioreactors. PLoS One 12 (7) e0181652.
Ko, M.K., Pellegrino, J.J., 1992. Determination of osmotic pressure and fouling resistance and their effects of performance of ultrafiltration membranes. J. Membr. Sci. 74 (1), 141–157.
Kundukad, B., Seviour, T., Liang, Y., Rice, S.A., Kjelleberg, S., Doyle, P.S., 2016. Mechanical properties of the superficial biofilm layer determine the architecture of biofilms. Soft Matter 12 (26), 5718–5726.
León Ohl, A., Horn, H., Hempel, D.C., 2004. Behaviour of biofilm systems under varying hydrodynamic conditions. Water Sci. Technol. 49 (11–12), 345–351.
Li, C., Wagner, M., Lackner, S., Horn, H., 2016. Assessing the influence of biofilm surface roughness on mass transfer by combining optical coherence tomography and two-dimensional modeling. Biotechnol. Bioeng. 113 (5), 989–1000.
MacMinn, C.W., Dufresne, E.R., Wettlaufer, J.S., 2016. Large deformations of a soft porous material. Phys. Rev. Appl. 5 (4), 044020.
Martin, K.J., Bolster, D., Derlon, N., Morgenroth, E., Nerenberg, R., 2014. Effect of fouling layer spatial distribution on permeate flux: a theoretical and experimental study. J. Membr. Sci. 471, 130–137.
McCarthy, A.A., Walsh, P.K., Foley, G., 2002. Experimental techniques for quantifying the cake mass, the cake and membrane resistances and the specific cake resistance during crossflow filtration of microbial suspensions. J. Membr. Sci. 201 (1), 31–45.
McDonogh, R., Schaule, G., Flemming, H.-C., 1994. The permeability of biofouling layers on membranes. J. Membr. Sci. 87 (1), 199–217.
Murga, R., Stewart, P.S., Daly, D., 1995. Quantitative analysis of biofilm thickness variability. Biotechnol. Bioeng. 45 (6), 503–510.
Okabe, S., Hiratia, K., Ozawa, Y., Watanabe, Y., 1996. Spatial microbial distributions of nitrifiers and heterotrophs in mixed-population biofilms. Biotechnol. Bioeng. 50 (1), 24–35.
Okabe, S., Kuroda, H., Watanabe, Y., 1998. Significance of biofilm structure on transport of inert particulates into biofilms. Water Sci. Technol. 38 (8), 163–170.
Picioreanu, C., Blauert, F., Horn, H., Wagner, M., 2018. Determination of mechanical properties of biofilms by modelling the deformation measured using optical coherence tomography. Water Res. 145, 588–598.
Poorasgari, E., Farsi, A., Christensen, M.L., 2016. Fouling of a microfiltration membrane by humic-like substances: a mathematical approach to modelling permeate flux and membrane retention. Water Sci. Technol. 73 (12), 3033–3040.
Poorasgari, E., Vistisen Bugge, T., Lykkegaard Christensen, M., Koustrup Jørgensen, M., 2015. Compressibility of fouling layers in membrane bioreactors. J. Membr. Sci. 475, 65–70.
Radu, A.I., Vrouwenvelder, J.S., van Loosdrecht, M.C.M., Picioreanu, C., 2010. Modeling the effect of biofilm formation on reverse osmosis performance: flux, feed channel pressure drop and solute passage. J. Membr. Sci. 365 (1), 1–15.
Radu, M., Bou-Said, B., Cicone, T., 2015. Experimental determination of viscoelastic properties of a highly compressible porous materials imbibed with water. Mech. Ind. 16 (6), 606.
Rosenthal, A.F., Griffin, J.S., Wagner, M., Packman, A.I., Balogun, O., Wells, G.F., 2018. Morphological analysis of pore size and connectivity in a thick mixed-culture biofilm. Biotechnol. Bioeng. 115 (9), 2268–2279.
Valladares Linares, R., Wexler, A.D., Bucs, S.S., Dreszer, C., Zwijnenburg, A., Flemming, H.C., Kruithof, J.C., Vrouwenvelder, J.S., 2015. Compaction and relaxation of biofilms. Desalination Water Treat. 57 (28), 12902–12914.
Wagner, M., Taherzadeh, D., Haisch, C., Horn, H., 2010. Investigation of the mesoscale structure and volumetric features of biofilms using optical coherence tomography. Biotechnol. Bioeng. 107 (5), 844–853.
Wang, Y., Fortunato, L., Jeong, S., Leiknes, T., 2017. Gravity-driven membrane system for secondary wastewater effluent treatment: filtration performance and fouling characterization. Separ. Purif. Technol. 184, 26–33.
Zhang, T.C., Bishop, P.L., 1994. Density, porosity, and pore structure of biofilms. Water Res. 28 (11), 2267–2277.
Zhang, T.C., Bishop, P.L., Gibbs, J.T., 1994. Effect of roughness and thickness of biofilms on external mass transfer resistance. In: Critical Issues inWater and Wastewater Treatment. National Conference in Environmental Engineering. ASCE, New York, pp. 593–600.